

Vector magnetometry based on electromagnetically induced transparency in linearly polarized light

V. I. Yudin,^{1,2,3,*} A. V. Taichenachev,^{1,2} Y. O. Dudin,⁴ V. L. Velichansky,^{5,6} A. S. Zibrov,⁷ and S. A. Zibrov^{6,†}

¹*Institute of Laser Physics, Siberian Branch of RAS, Novosibirsk 630090, Russia*

²*Novosibirsk State University, Novosibirsk 630090, Russia*

³*Novosibirsk State Technical University, Novosibirsk 630092, Russia*

⁴*School of Physics, Georgia Institute of Technology, Atlanta, Georgia 30332-0430, USA*

⁵*Moscow State Engineering and Physics Institute, Moscow 115409, Russia*

⁶*Lebedev Physical Institute, RAS, Moscow 117924, Russia*

⁷*Physics Department, Harvard University, Cambridge, Massachusetts 02138, USA*

(Received 21 May 2010; published 13 September 2010)

We develop a generalized principle of electromagnetically induced transparency (EIT) vector magnetometry based on high-contrast EIT resonances and the symmetry of atom-light interaction in the linearly polarized bichromatic fields. Operation of such vector magnetometer on the D_1 line of ^{87}Rb has been demonstrated. The proposed compass-magnetometer has an increased immunity to shifts produced by quadratic Zeeman and ac-Stark effects, as well as by atom-buffer gas and atom-atom collisions. In our proof-of-principle experiment the detected angular sensitivity to magnetic field orientation is 10^{-3} deg/Hz $^{1/2}$, which is limited by laser intensity fluctuations, light polarization quality, and magnitude of the magnetic field.

DOI: [10.1103/PhysRevA.82.033807](https://doi.org/10.1103/PhysRevA.82.033807)

PACS number(s): 42.50.Gy, 07.55.Ge, 32.30.Dx, 32.70.Jz

I. INTRODUCTION

The pure quantum state is a basic concept of quantum physics, which plays a key role in various applications, such as magnetometry, frequency standards, laser cooling, quantum information science, nonlinear optics, and “slow” and “fast” light experiments. The effect of electromagnetically induced transparency (EIT) [1–4] has been successfully employed in all these applications.

The idea of EIT scalar magnetometer has been suggested in [5]. The steep dispersion of EIT media promises a dramatic improvement of the scalar magnetometer sensitivity. Since then different schemes for EIT magnetometry have been considered. Among them are schemes based on the nonlinear Faraday effect in a manifold of a single ground state [6–8] and a scheme in which the frequency shift of Zeeman sublevels of both ground states is detected [9]. The sensitivity of EIT magnetometers is in the same range as magnetometers using optical pumping [10,11]. The recent modification of optically pumped magnetometers with suppressed spin-exchange broadening (so-called SERF magnetometer) drastically improves sensitivity by a factor of 10^3 . It overcomes the sensitivity of SQUID magnetometers (10^{-15} T/Hz $^{1/2}$) [12]. Unfortunately, SERF magnetometers work in small fields that are less than $0.1 \mu\text{T}$, which is significantly weaker than geomagnetic field.

For many applications it is preferable to know not only the scalar, but also the direction of the magnetic field. To achieve this, individual coils are installed for each of the X , Y , and Z axes in a scalar magnetometer. The coils are used to induce small modulations of the magnetic field along each axis, which gives the information about B_x and B_y field

components [13–15]. This allows the orientation of the vector \mathbf{B} to be reconstructed. The first EIT vector magnetometer schemes have been proposed in [16,17]. However, the angular accuracy of these schemes strongly depends on mathematical models (describing the atom-field interaction and light field propagation) used to extract the magnetic field direction from experimental signals. The vector magnetometer using the nonlinear magneto-optical rotation has been investigated in [18], where the angular sensitivity 3.8×10^{-3} deg/Hz $^{1/2}$ was achieved. The similar method was theoretically studied in [19]. In the paper [20] the single-ion magnetic compass was considered. The reviews of existing all-optical magnetometers were published in [11,21].

In the present paper we show that employing the unique features of high-contrast EIT resonances on the D_1 line of ^{87}Rb allows us to find new approaches to the atomic vector magnetometry and to model a relevant device in which the scalar and vector properties of magnetic field can be measured separately or simultaneously. Our approach does not require the mathematical models to reconstruct a three-dimensional (3D) orientation of the magnetic field.

II. GENERAL DESCRIPTION OF THE PROBLEM

The EIT phenomenon is closely connected to the so-called coherent population trapping (CPT) [1,2] in which an atom-field interaction of the pure quantum state $|\text{dark}\rangle$ is zero:

$$-(\hat{\mathbf{d}} \cdot \mathbf{E})|\text{dark}\rangle = 0, \quad (1)$$

where $\hat{\mathbf{d}}$ is the operator of atomic dipole moment and \mathbf{E} is the electric field vector. The state (1) is a special coherent superposition of the ground-state Zeeman sublevels that neither absorbs nor emits light. Dark states lead to the highest contrast of EIT resonances. Thus, the preparation of pure states is crucial for any of the previously mentioned applications.

*viyudin@mail.ru

†serezha.zibrov@gmail.com

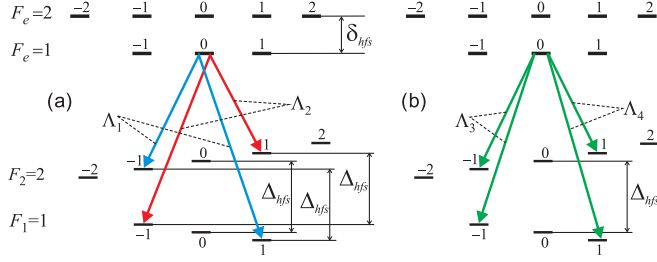


FIG. 1. (Color online) Pure Λ systems at the D_1 line of ^{87}Rb ; nonsensitive (a) and sensitive (b) to magnetic field. Here we do not show Zeeman shifts for upper hyperfine levels with $F_e = 1, 2$.

The generalized problem of the production of pure quantum states by bichromatic elliptically polarized field was solved in [22]. In [23–25] it was theoretically and experimentally demonstrated that the D_1 line of ^{87}Rb has unique level structure for the production of pure dark states using bichromatic linearly polarized light (so-called lin||lin field), where the resonant interaction occurs via the upper energy level $F_e = 1$. There are two pairs of dark states, where each dark state corresponds to the separate Λ scheme (see Fig. 1). One pair corresponds to Λ_1 and Λ_2 schemes in Fig. 1(a) and involves the following two-photon transitions: $|F_1 = 1, m = -1\rangle \leftrightarrow |F_2 = 2, m = +1\rangle$ and $|F_1 = 1, m = +1\rangle \leftrightarrow |F_2 = 2, m = -1\rangle$. In our experiments the EIT resonances of these pairs have a high contrast (50%) and transmission (60%) (solid line in Fig. 2). Both Λ_1 and Λ_2 transitions contribute to EIT resonance (the dependence of transmission on the difference of the two optical frequencies) that is attractive for applications in chip-size atomic clocks (CSAC) since it provides high contrast and smaller (by factor 1.33) quadratic dependence on the magnetic field compared to the regular atomic clock transition $|F_1 = 1, m = 0\rangle \leftrightarrow |F_2 = 2, m = 0\rangle$ [26–28]. Note that the shifts of zero magnetic sublevels and the frequency of 0-0 transition do not depend linearly on magnetic field, while sublevels with $m = \pm 1$ do. The electron g factors of the ground states $F_{1,2}$ have the same magnitude but *opposite signs* (see Fig. 1). As a result, the residual linear shifts (due to a nuclear contribution) of the Λ_1 and Λ_2 transitions are 250 times smaller than the shifts of individual magnetic sublevels

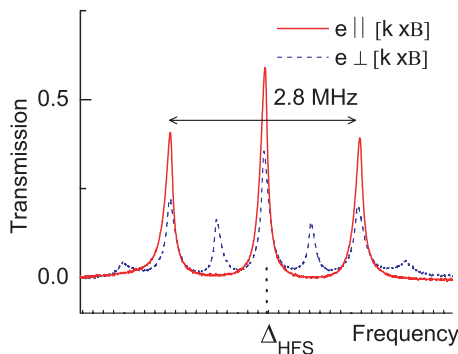


FIG. 2. (Color online) EIT resonance transmission. Solid line: The case $\mathbf{e} \parallel \mathbf{n}$. The central resonance corresponds to the Λ_1 and Λ_2 schemes [Fig. 1(a)]. This resonance has 120-kHz width and $\sim 60\%$ transmission. Dashed line: The case $\mathbf{e} \perp \mathbf{n}$. The magnetic field has magnitude 1 G; the angle between \mathbf{B} and \mathbf{k} equals 20° .

$m = \pm 1$ ($\approx \pm 28 \text{ Hz}/\mu\text{T}$ instead of $\approx \pm 7 \text{ kHz}/\mu\text{T}$). However, these residual shifts are manifested only in a small broadening of the resonance lineshape, while the center of the resulting $\Lambda_{1,2}$ resonance has a zero linear sensitivity to the magnetic field (due to the symmetry of Λ_1 and Λ_2 systems for the lin||lin light) [23,24].

The other pair of Λ schemes [Λ_3 and Λ_4 in Fig. 1(b)] gives the two-photon transitions: $|F_2 = 2; m = -1\rangle \leftrightarrow |F_1 = 1; m = -1\rangle$ and $|F_2 = 2; m = +1\rangle \leftrightarrow |F_1 = 1; m = +1\rangle$ that strongly depend on magnetic field and can be used for measurement of the magnetic field magnitude, as it was noted in [24].

To produce quantum dark states (1) for the D_1 line of ^{87}Rb , we use (in conformity with [23,24]) a linearly polarized bichromatic running wave $\mathbf{E}(\mathbf{r}, t)$ with close frequencies ω_1 and ω_2 and wave vector \mathbf{k} (i.e., lin||lin configuration):

$$\mathbf{E}(\mathbf{r}, t) = (E_1 e^{-i\omega_1 t} + E_2 e^{-i\omega_2 t}) e^{i\mathbf{k}\cdot\mathbf{r}} \mathbf{e} + \text{c.c.}, \quad (2)$$

where \mathbf{e} is a unit vector of the linear polarization, and $E_{1,2}$ are the scalar amplitudes of the corresponding frequency components. The interaction occurs in the presence of the static magnetic field \mathbf{B} . If the z axis is directed along the vector \mathbf{B} , the vector \mathbf{e} can be expressed in a spherical basis $\{\mathbf{e}_0 = \mathbf{e}_z, \mathbf{e}_{\pm 1} = \mp(\mathbf{e}_x \pm i\mathbf{e}_y)/\sqrt{2}\}$:

$$\mathbf{e} = \sum_{q=0,\pm 1} e^{(q)} \mathbf{e}_q = (\cos \theta) \mathbf{e}_0 - \frac{\sin \theta}{\sqrt{2}} (\mathbf{e}_{+1} - \mathbf{e}_{-1}), \quad (3)$$

where θ is the angle between vectors \mathbf{B} and \mathbf{e} ; $e^{(q)}$ are the contravariant components of the vector \mathbf{e} . Note that for linear polarization its circular components (σ_{\pm}) are always equal:

$$|e^{(+1)}| = |e^{(-1)}| = |\sin \theta|/\sqrt{2}. \quad (4)$$

As will be shown in the following, the symmetry (4) is one of the principal points of EIT magnetometry in a linear polarized field.

In the resonant approximation we assume that the frequency component ω_j ($j = 1, 2$) excites atoms only from the hyperfine ground level F_j (Fig. 1). From here on, we use the interaction representation,

$$e^{-i\mathcal{E}_{F_m} t/\hbar} |F, m\rangle \rightarrow |F, m\rangle,$$

where \mathcal{E}_{F_m} is the energy of the level $|F, m\rangle$ in which the Zeeman shift is included. The operator of an atom-field interaction $-(\hat{\mathbf{d}} \cdot \mathbf{E}) = \hat{V} + \hat{V}^\dagger$ under the resonant approximation takes the form

$$\begin{aligned} \hat{V} = & e^{i\mathbf{k}\cdot\mathbf{r}} \sum_{q=0,\pm 1} e^{(q)} \\ & \times \left[E_1 \sum_{F_e, \mu, m_1} d_{F_e F_1} e^{-i\delta_{\mu m_1}^{(1)} t} C_{F_1 m_1, 1q}^{F_e \mu} |F_e, \mu\rangle \langle F_1, m_1| \right. \\ & \left. + E_2 \sum_{F_e, \mu, m_2} d_{F_e F_2} e^{-i\delta_{\mu m_2}^{(2)} t} C_{F_2 m_2, 1q}^{F_e \mu} |F_e, \mu\rangle \langle F_2, m_2| \right]. \end{aligned} \quad (5)$$

Here, $d_{F_e F_1}$ and $d_{F_e F_2}$ denote reduced matrix elements of corresponding optical transitions $F_1 \rightarrow F_e$ and $F_2 \rightarrow F_e$, $C_{F_j m_j, 1q}^{F_e \mu}$ are Clebsch-Gordan coefficients, and $\delta_{\mu m_j}^{(j)} = \omega_j -$

$(\mathcal{E}_{F_e\mu} - \mathcal{E}_{F_j m_j})/\hbar$ for $j = 1, 2$ are corresponding one-photon detunings.

For alkali-metal atoms with nuclear spin I_n we have $F_1 = (I_n - 1/2)$ and $F_2 = (I_n + 1/2)$. The corresponding electron ground-state Landé factors have the same absolute value but opposite signs: $g = -g_{F_1} = g_{F_2} = (I_n + 1/2)^{-1}$ (for ^{87}Rb $g = 1/2$). Then in the linear approximation of the dependence on the magnetic field \mathbf{B} and neglecting the nuclear magneton contribution it is easy to count the number of split two-photon resonances. For arbitrary directed \mathbf{B} there are $(4I_n + 1)$ two-photon resonances in transmissions versus Raman detuning $\delta_R = (\omega_1 - \omega_2 - \Delta_{hfs})$ dependencies centered at the points $\delta_R = l g \mu_B |\mathbf{B}|/\hbar$ ($l = -2I_n, \dots, 2I_n$), where μ_B is Bohr magneton. For example, in ^{87}Rb ($I_n = 3/2$) we have seven two-photon resonances (the blue dashed line in Fig. 2). In the particular case of $\mathbf{B} \perp \mathbf{e}$, the number of two-photon resonances equals to $2I_n = 3$ (the red solid line in Fig. 2).

III. EIT-BASED 3D COMPASS

First we examine in detail the central resonance (near $\delta_R = 0$). It will be shown below that this resonance can be used for the vector magnetometer due to the strong dependence of transmission on the mutual orientation of vectors \mathbf{e} and \mathbf{B} [i.e., on the angle θ in Eq. (3)]. The following two transitions take place in formation of the central two-photon resonance: $|F_1, m = -1\rangle \leftrightarrow |F_2, m = +1\rangle$ and $|F_1, m = +1\rangle \leftrightarrow |F_2, m = -1\rangle$, for which the energy difference equals $\hbar \Delta_{hfs}$ [Fig. 1(a)]. The third two-photon transition $|F_1, m = 0\rangle \leftrightarrow |F_2, m = 0\rangle$ (between magnetically insensitive sublevels) is strongly suppressed due to further destructive interference of contributions from the opposite circular components σ_{\pm} .

In the case of a resolved upper hyperfine structure ($F_e = 1, 2$ in the Fig. 1), the two-photon resonance can be excited via separate level. Further we assume that the frequency components (2) are at the resonance with a single hyperfine level $F_e = 1$ (Fig. 1). Now let us consider a special case where the vectors \mathbf{e} and \mathbf{B} are mutually orthogonal ($\theta = \pi/2$), and, therefore, only two equal circular components $\mathbf{e} = -(\mathbf{e}_{+1} - \mathbf{e}_{-1})/\sqrt{2}$ occur in the decomposition (3). It is seen from Fig. 1(a) that there is a two-photon resonance formed via pure Λ_1 scheme with Zeeman sublevels $|F_1 = 1, m = +1\rangle$ and $|F_2 = 2, m = -1\rangle$. Similarly, the Λ_2 scheme is realized with the other sublevel pairs $|F_1 = 1, m = -1\rangle$ and $|F_2 = 2, m = +1\rangle$. Both of these $\Lambda_{1,2}$ schemes are formed via the same common upper sublevel $|F_e = 1, m = 0\rangle$. As was mentioned before, the frequencies of these two-photon resonances are equal (neglecting the nuclear magneton contribution) to the frequency of the (0-0) resonance between sublevels $|F_1 = 1, m = 0\rangle$ and $|F_2 = 2, m = 0\rangle$.

The uniqueness of the situation arises from overlapping the two dark states $|\text{dark}\rangle_{\Lambda_1}$ and $|\text{dark}\rangle_{\Lambda_2}$, which occur at the two-photon resonance, $\delta_R = 0$. These states satisfy Eq. (1) and have the following forms:

$$|\text{dark}\rangle_{\Lambda_{1,2}} = \frac{\sqrt{3}E_2|F_1, m = \pm 1\rangle \mp E_1|F_2, m = \mp 1\rangle}{\sqrt{|E_1|^2 + 3|E_2|^2}}. \quad (6)$$

The presence of such dark states in the $\mathbf{e} \perp \mathbf{B}$ case leads to a high contrast of the central dark resonance near $(\omega_1 - \omega_2) =$

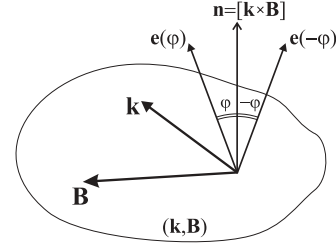


FIG. 3. Orientation of the magnetic field \mathbf{B} , wave vector \mathbf{k} , and polarization \mathbf{e} of the optical field.

Δ_{hfs} (i.e., $\delta_R \approx 0$). This fact was predicted and experimentally demonstrated in [23,24].

In the general case of $\theta \neq \pi/2$ [i.e., $\cos(\theta) \neq 0$] there are no pure Λ schemes due to the π -polarized (along \mathbf{B}) component in decomposition (3). It leads to a smaller amplitude and contrast of the central two-photon $\Lambda_{1,2}$ resonance in comparison to the case of $\theta = \pi/2$. This fact will be used as a basis for determination of the magnetic field orientation (i.e., compass) in our approach.

The basic idea of our method can be explained in the following way. Assume that the wave vector \mathbf{k} and the vector \mathbf{B} have an arbitrary mutual orientation. We will use the amplitude of the central resonance (absorption, transmission, or fluorescence) as the measured quantity (Fig. 2). There are two cases, where \mathbf{e} and \mathbf{B} are orthogonal to each other. More precisely, these situations arise if $\mathbf{e} \parallel \mathbf{n}$, where $\mathbf{n} = [\mathbf{k} \times \mathbf{B}]$ (Fig. 3). These cases correspond to the dark states (6), which leads to the maximal amplitude and contrast of the central resonance (as explained previously).

Consider the dependence of the dark resonance amplitude, which is obtained by rotating the polarization vector \mathbf{e} around fixed wave vector \mathbf{k} . This dependence can be presented as a function $A_{\mathbf{k}}(\varphi)$, where φ is the angle between the vectors \mathbf{e} and \mathbf{n} (Fig. 3). Even the qualitative analysis, provided above, leads to the conclusion that the function $A_{\mathbf{k}}(\varphi)$ reaches its maximum at $\varphi = 0, \pi$ (i.e., when $\mathbf{e} \perp \mathbf{B}$).

The essence of the measuring procedure could be represented by the following algorithm. At first, for a chosen vector $\mathbf{k} = \mathbf{k}_1$, we get the $A_{\mathbf{k}_1}(\varphi)$ dependence by rotating the polarization vector \mathbf{e} around wave vector \mathbf{k}_1 . The maximum of this dependence corresponds to the direction of the vector $\mathbf{n} = [\mathbf{k}_1 \times \mathbf{B}]$, which gives us the equation for the plane $(\mathbf{k}_1, \mathbf{B})$ formed by the vectors \mathbf{k}_1 and \mathbf{B} . Repeating the same procedure for another orientation of the wave vector $\mathbf{k} = \mathbf{k}_2$ (e.g., $\mathbf{k}_2 \perp \mathbf{k}_1$) provides the equation for the plane $(\mathbf{k}_2, \mathbf{B})$. The intersection line of the two planes $(\mathbf{k}_1, \mathbf{B})$ and $(\mathbf{k}_2, \mathbf{B})$ gives the 3D orientation of the vector \mathbf{B} with an uncertainty of the sign.

The basic principle of our method is quite universal and does not depend on different experimental parameters (such as the $|E_1/E_2|$ ratio, one-photon detuning, relaxation constants, atom-atom collisions, nuclear magnetic momentum, and so on). This can be seen from the general symmetry of the problem. Indeed, suppose we have an arbitrary polychromatic wave propagating along a direction \mathbf{k} and having the same linear polarization \mathbf{e} for all frequency components. Also we assume that the atomic medium is isotropic in the absence of the light field. We determine the signal $S(\mathbf{e}, \mathbf{B})$ as a scalar value

that depends on the mutual orientation of the vectors \mathbf{e} and \mathbf{B} . In the sense of this definition, $S(\mathbf{e}, \mathbf{B})$ could be the transmission, absorption, or fluorescence. A general analysis of the Bloch equations gives the following relationship:

$$S(\mathbf{e}, \mathbf{B}) = S(\mathbf{e}, -\mathbf{B}) = S(-\mathbf{e}, \mathbf{B}). \quad (7)$$

The left equality comes from the symmetry of Clebsch-Gordan coefficients $|C_{Fm, 1q}^{F'm'}| = |C_{F-m, 1-q}^{F'-m'}|$ and the equality of the circular components (4) in an arbitrary coordinate system. The right equality in (7) arises due to an independence of the $S(\mathbf{e}, \mathbf{B})$ on field phase (the transmission and absorption depend on the $|\mathbf{E}|^2$).

Consider a configuration shown in Fig. 3, where the light field has $\mathbf{e}(\varphi)$ polarization. Let us perform a mathematical reflection in relation to the plane (\mathbf{k}, \mathbf{B}) . This leads to the substitution of the polarization vector $\mathbf{e}(\varphi) \rightarrow [-\mathbf{e}(-\varphi)]$, but for the *pseudovector* of the magnetic field it leads to $\mathbf{B} \rightarrow (-\mathbf{B})$. It is known that the mathematical reflection does not affect a scalar signal (i.e., another relationship is obtained):

$$S(\mathbf{e}(\varphi), \mathbf{B}) = S(-\mathbf{e}(-\varphi), -\mathbf{B}). \quad (8)$$

By combining (7) and (8) we finally achieve

$$S(\mathbf{e}(\varphi), \mathbf{B}) = S(\mathbf{e}(-\varphi), \mathbf{B}), \quad (9)$$

(i.e., the scalar signal is an even function of the angle φ). It means that the points $\varphi = 0, \pi$ (i.e., $\mathbf{e} \perp \mathbf{B}$) correspond to the local extremum (maximum or minimum) of the $S(\mathbf{e}(\varphi), \mathbf{B})$ dependence, which is obtained by rotating the polarization vector \mathbf{e} around wave vector \mathbf{k} . Similar symmetry consideration shows that there are two other extremuma when the vector \mathbf{e} lies in the plane (\mathbf{k}, \mathbf{B}) (i.e., at $\varphi = \pm\pi/2$). Note that the derived results remain valid in the case of light wave propagation (including the nonlinear effects in an optically thick medium). In this case the previously used vector $\mathbf{e}(\varphi)$ corresponds to the initial linear polarization before atomic medium (cell).

Thus, we have shown that the described principle of EIT vector magnetometry is valid, in essence, for arbitrary atoms, lines (D_1 or D_2), and arbitrary spectral composition of linearly polarized wave (including a monochromatic wave). However, the dependence $A_{\mathbf{k}}(\varphi)$ for the central resonance excited by a bichromatic field at the ^{87}Rb D_1 line is the best choice for the demonstration of the compass principle because of the significant signal-to-noise ratio (S/N) and transmission.

EIT vector magnetometry in a circularly polarized light has been discussed in [16,17]. In those schemes the mathematical models (density matrix and Maxwell equations) are required to reconstruct the vector of the magnetic field from experimental signals. Meanwhile, any model is sensitive to the ultimate knowledge of involved parameters and processes, such as: light intensities, one-photon detunings, light beam profile, atomic density, atomic diffusion motion in buffer gas, collision processes (depolarization, broadening, shifts), and so on. This may limit and sufficiently decrease the achievable angular accuracy (to the level of 1° – 10°) of the vector magnetometer. In contrast, our 3D compass does not require the use of mathematical models, because the extremum of the angle dependence $A_{\mathbf{k}}(\varphi)$ at the points $\varphi = 0, \pi$ is an inherent feature.

IV. EIT SCALAR MAGNETOMETER

As was shown above, rotating the linear polarization \mathbf{e} around the wave vector \mathbf{k} and analyzing the corresponding dependence of amplitude $A_{\mathbf{k}}(\varphi)$ of the central dark resonance, we always can find the condition $\mathbf{e} \perp \mathbf{B}$. In this section we will consider two-end magnetically sensitive resonances (Fig. 2, red solid line), which are connected with $\Lambda_{3,4}$ systems shown in Fig. 1(b) [i.e., with two-photon transitions $(-1) \leftrightarrow (-1)$ and $(+1) \leftrightarrow (+1)$]. In the $\mathbf{e} \perp \mathbf{B}$ case, the amplitudes of these resonances attain maximum, too, because at the exact two-photon resonance (i.e., $\delta_R = \pm 2g\mu_B |\mathbf{B}|/\hbar$) there are the following two dark states:

$$|\text{dark}\rangle_{\Lambda_{3,4}} = \frac{\sqrt{3}E_2|F_1, m = \mp 1\rangle \pm E_1|F_2, m = \mp 1\rangle}{\sqrt{|E_1|^2 + 3|E_2|^2}}. \quad (10)$$

We can determine the value $|\mathbf{B}|$ by measuring the distance between these resonances $|\Delta_{\pm}|$. In the linear approximation for $|\mathbf{B}|$ we apply the formula $|\Delta_{\pm}| = \gamma'|\mathbf{B}|$, where $\gamma' = 2(g_{F_2} - g_{F_1})\mu_B/\hbar$ is an effective gyromagnetic ratio. Due to the effect of the nuclear magneton for ^{87}Rb [29,30] we should use the following values for g factors: $g_{F_1} = -0.501\,827$ and $g_{F_2} = 0.499\,836$. Thus, in our case, $\gamma' = 2.803\,905 \times 10^{10}$ Hz/T.

Taking into account the symmetry of the atom-light interactions in the linear polarization one can predict some important properties of such magnetometry scheme. Indeed, this frequency-differential magnetometer is immune to: (I) the collisional shift arising due to interactions with an isotropic buffer gas; (II) the quadratic Zeeman shift of magnetic sublevels; (III) the shift arising from atom-atom interactions (including spin exchange) between atoms (here between ^{87}Rb atoms); and (IV) the ac-Stark shift.

The property (I) is a result of the equality of the collisional shifts of all Zeeman sublevels $|F, m\rangle$ (for a given F) in an isotropic buffer gas. The property (II) is also quite obvious considering that each even on $|\mathbf{B}|$ power of the Zeeman shift has an equal value and sign for the $m \leftrightarrow m$ and $(-m) \leftrightarrow (-m)$ transitions. This feature is valid for any atom (i.e., not only for ^{87}Rb) and line (D_1 and D_2).

The property (III) is a result of the interaction of atoms with linear polarized light. Indeed, let us consider the atomic density matrix $\hat{\rho}$, which describes the distribution among Zeeman sublevels:

$$\hat{\rho} = \sum_{F', m', F'', m''} \rho_{m'm''}^{F'F''} |F', m'\rangle \langle F'', m''|, \quad (11)$$

where $\rho_{m'm''}^{F'F''}$ are matrix elements. We denote the atomic distribution for two-photon resonances $(+1) \leftrightarrow (+1)$ and $(-1) \leftrightarrow (-1)$ (at the $\delta_R = \pm g\mu_B |\mathbf{B}|$) as $\rho_{m'm''}^{(+)F'F''}$ and $\rho_{m'm''}^{(-)F'F''}$, respectively. From the general symmetry and neglecting some insignificant details (e.g., a small variation of the one-photon detuning) we get $|\rho_{m'm''}^{(+)F'F''}| = |\rho_{-m'-m''}^{(-)F'F''}|$. Obviously, this relationship is not changed by the atom-atom interactions (including the spin-exchange process). Therefore, the corresponding collisional frequency shifts have the same magnitude, that is, they do not affect the frequency difference Δ_{\pm} (while the collisional *broadening* of the EIT resonances will have an influence). This property gives a significant advantage in comparison with other schemes of atomic magnetometers,

where the atom-atom interaction is a limiting factor for precise magnetic field measurements. The property (III) also supports the use of miniature-size cells in our EIT magnetometer because it is possible to work at high cell temperature to get high atomic density.

Note that the property (III) can be extended to an arbitrary element (i.e., not only ^{87}Rb) and resonance line, when the magnetometer uses the frequency difference between two-photon resonances $m \leftrightarrow m$ and $(-m) \leftrightarrow (-m)$. In general, the angle θ (between vectors \mathbf{B} and \mathbf{e}) can be arbitrary.

The property (IV) follows from two circumstances. Firstly, the light shifts of two-photon resonances (see Fig. 2, red solid line) that occur via upper level $F_e = 1$ are absent, because the dark states nullify the resonant interaction (1). Therefore, these ac-Stark shifts are small and appear mostly due to the interaction with the far-off-resonance level $F_e = 2$; see Fig. 1. Secondly, due to the symmetry, these shifts are practically identical and compensate each other (in the value Δ_{\pm}). There is, however, a small imbalance caused by Zeeman splitting (Δ_Z). This splitting leads to a small difference for all one-photon detunings near the dark resonances $(+1) \leftrightarrow (+1)$ and $(-1) \leftrightarrow (-1)$. Thus, if the value of the light shift for extreme resonances is approximately U , then the relative shift can be estimated as $\sim |\Delta_Z/\delta_{hfs}||U|$, which means an additional significant suppression of shift by the factor $|\Delta_Z/\delta_{hfs}| \ll 1$. Note that similar advantages of the optically pumped balance magnetometer also have been pointed out in [31].

In our case the magnetometer sensitivity δB depends on the signal-to-noise ratio of the Zeeman resonance signal and the width of the EIT resonance Γ_{FWHM} : $\delta B = \Delta B/(S/N)$, where $\Delta B = \Gamma_{\text{FWHM}}/\gamma'$. Therefore, a high contrast of the Λ resonances, where most of the atoms (50%–70%) are accumulated in the dark state [23–25], makes them a perspective competitor for existing all-optical magnetometers [21]. As an example, we estimate the achievable sensitivity using recently published data on the $|\text{lin}\rangle|\text{lin}\rangle$ resonances [26] (authors of [26] characterized the $|\text{lin}\rangle|\text{lin}\rangle$ resonances as an atomic clock reference). With a resonance width $\Gamma_{\text{FWHM}} = 900$ Hz and $S/N = 3300$ Hz $^{1/2}$, the sensitivity for the measurable magnetic field is $\delta B < 10^{-11}$ T/Hz $^{1/2}$, which can be obtained without special efforts and for very moderate density 10^{10} cm $^{-3}$ of rubidium atoms (50°C and 1.2 Torr N_2 pressure in [26]). To significantly improve the sensitivity one should increase the number of atoms. In this case the EIT differential magnetometer will achieve sensitivity at the level $\delta B \sim 10^{-13}$ – 10^{-14} T/Hz $^{1/2}$ or better, because we expect to reach an atom concentration greater than 10^{12} cm $^{-3}$ without serious limitations due to collisional processes [property (III)]. The proper choice of buffer gas pressure and the additional narrowing of EIT resonance in dense media [32,33] also gives some advantages. However, it is worth noting that the behavior of the coherent effects (EIT) in dense vapor $>10^{12}$ cm $^{-3}$ has not yet been studied in detail, though it is known that at 10^{14} cm $^{-3}$ EIT is still observed [34].

Additionally, we note that each of Λ_3 and Λ_4 resonances [i.e., $(-1) \leftrightarrow (-1)$ and $(+1) \leftrightarrow (+1)$ two-photon transitions] can be used also in the compass scheme (described in the previous section). But it has some drawbacks in comparison with the compass based on the central resonance (i.e., $\Lambda_{1,2}$). Firstly, the frequency position of each of these resonances

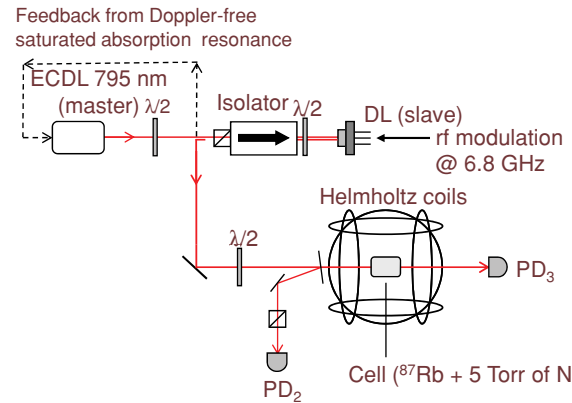


FIG. 4. (Color online) The schematic of the experimental setup.

depends on the magnetic field. Secondly, their transmission dependence $A_{\mathbf{k}}(\varphi)$ versus rotation of the vector $\mathbf{e}(\varphi)$ can have two local maxima. One of them (which always exists) corresponds to the case $\mathbf{e} \perp \mathbf{B}$, but the other possible maximum emerges, when the vector \mathbf{e} lies in the plane (\mathbf{k}, \mathbf{B}) . Such situation leads to an uncertainty in the measurement procedure.

V. EXPERIMENT

From our point of view the possibility of an EIT-based compass is the most attractive and unusual part of the suggested ideas. Therefore, in the experimental part we just concentrate on this idea. The experimental setup is shown in Fig. 4. The bichromatic field $\mathbf{E}(\mathbf{r}, t)$ is delivered by an extended cavity (ECDL) and injected into the slave diode laser (DL); frequency is modulated at $\Delta_{hfs} = 6.8$ GHz [24]. The experiment is carried out with a Pyrex cell (40-mm long and 25 mm in diameter) containing isotopically enriched ^{87}Rb and 5 Torr neon buffer gas. The cell is placed inside Helmholtz coils, where the field inhomogeneity is ~ 2 mG/cm. For the experiments reported here the cell temperature is 45°C.

The laser frequency is locked to the Doppler-free saturated absorption resonance. The radiation power at the cell front window is 1.5 mW. To excite the $\Lambda_{1,2}$ scheme, the carrier frequency is tuned to the $F_2 = 2 \rightarrow F_e = 1$ transition, and the high-frequency sideband is tuned to the $F_1 = 1 \rightarrow F_e = 1$ transition. The displayed spectra of the EIT resonances are shown in Fig. 2, where the curves correspond to the ^{87}Rb transmission spectra for the two cases $\mathbf{e} \parallel \mathbf{n}$ and $\mathbf{e} \perp \mathbf{n}$.

Before entering the cell, light passes through a half-wave plate, which is rotating at a 13-Hz rate. As a result, we detect the dependence of light transmission as a function of the angle φ between \mathbf{e} and \mathbf{n} ; see Fig. 5. It is worth noting that the light transmission is affected by changes of the EIT transmission and by variation of the Doppler absorption profile due to optical pumping. To avoid this distortion of the transmission we detect signals at the second harmonic of the rf-modulated polarization which is done by Faraday modulator at 7.6 kHz. To determine the detection sensitivity of the vector \mathbf{B} direction we change the orientation of the magnetic field in 0.1° steps. The lock-in amplifier output detects these steps, from which we estimate a sensitivity of $\sim 10^{-3}$ deg/Hz $^{1/2}$ (Fig. 6). These data were taken for $\mathbf{B} \perp \mathbf{k}$ at 1-G magnetic field with the detection bandwidth of 300 Hz.

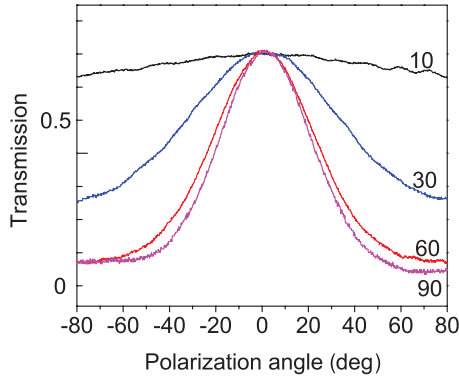


FIG. 5. (Color online) The dependence of the EIT-resonance amplitude $A_{\mathbf{k}}(\varphi)$ for the ^{87}Rb cell transmission on the angle φ between \mathbf{e} and \mathbf{n} . Angles between \mathbf{B} and \mathbf{k} are shown on the right side of each curve (both vectors lie in the horizontal plane).

We have found that the sensitivity depends on the magnitude of the applied magnetic field (Fig. 7). At low magnetic field the sensitivity decreases almost by two orders of value compared to that at 0.1–7 G. This occurs due to trap states belonging to the degenerate Zeeman sublevels of the same hyperfine level where atoms “hide.” The contrast (as well as signal-to-noise ratio) grows with the magnetic field. It is caused by lifting of the sublevel degeneracy. To destroy trap states, a magnetic field should be strong enough [i.e., such that the splitting between the (0-0) (i.e., $\Lambda_{1,2}$) and (1-1) (i.e., $\Lambda_{3,4}$) transitions greater than the EIT resonance width]. Once the (0-0) and (1-1) transitions are separated by ~ 0.1 G (in our setup), the compass has the best sensitivity for $|\mathbf{B}| > 1$ G. For some magnetic field ($|\mathbf{B}| > 5$ G in our experiments) the central resonance begins to split [23–25,35], because the Λ_1 and Λ_2 transitions have a small difference in g factors (± 2.8 kHz/G) due to the nuclear spin. However, this effect itself does not set the upper operational limit of the magnetic field for the vector measurements (compass), because in this case we can work with one of the two separated Λ resonances. We believe that the upper limitation on the magnetic field in our method is connected with the degradation of EIT resonances when the value $\mu_B|\mathbf{B}|$ is comparable with excited state hyperfine splitting $\delta_{hfs} \approx 812$ MHz (i.e., due to a strong magnetic mixing

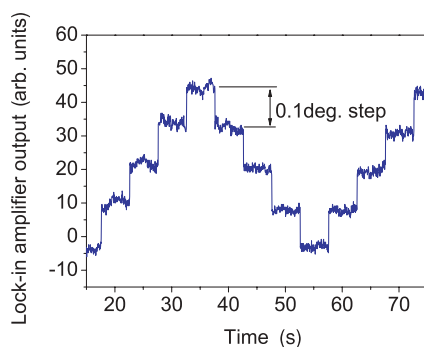


FIG. 6. (Color online) The lock-in amplifier output at 0.1° angle step variation of the magnetic field direction. The magnetic field magnitude is 1 G, and the angle between magnetic field and wave vector is varied near 90° .

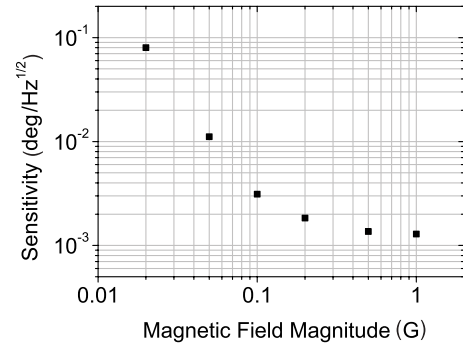


FIG. 7. Compass sensitivity versus magnetic field magnitude.

between upper hyperfine levels $F_e = 1$ and $F_e = 2$; see Fig. 1). In summary, for the parameters of our setup the magnetic field operational range of the 3D compass is about ~ 0.1 –200 G.

VI. CONCLUSION

In conclusion, we have developed the generalized principles of atomic vector magnetometry based on high-contrast EIT resonances in a linearly polarized field. These principles follow from a general symmetry of the problem and are valid for arbitrary atoms, transitions, and arbitrary spectral composition of linearly polarized wave (including a monochromatic wave). The compass involving two nonparallel laser beams allows one to measure the orientation of the magnetic field in three dimensions. In our proof-of-principle experiment we have achieved a compass sensitivity $\sim 10^{-3}$ deg/Hz $^{1/2}$ at intermediate magnetic fields. We have found that the major contribution to the noise-limiting sensitivity is related to intensity fluctuations of the laser system. Thus, we believe that the proposed method has a potential to achieve an angular sensitivity at the level of $\sim 10^{-4}$ deg/Hz $^{1/2}$. In contrast to other schemes of the vector EIT magnetometer, the proposed scheme does not depend on a completeness of the magnetometer mathematical model and gives a straight way to find the magnetic field direction and at the end provides a higher angular accuracy.

We have also discussed properties and advantages of the EIT scalar magnetometry, such as nonsensitivity to quadratic Zeeman and ac Stark effects, atom-buffer gas, and atom-atom collisions. Moreover, our scalar magnetometer works with a maximal sensitivity and an accuracy at the arbitrary mutual orientation of the vectors \mathbf{k} and \mathbf{B} , that is, “dead” zones are absent (see also [36]). The spatial resolution, sensitivity, dynamical range, and bandwidth of the magnetic field measurement can be varied by the proper choice of the cell volume, temperature, buffer gas type, and its pressure (or coating).

EIT vector magnetometers is important for noninvasive biomedical studies [37,38], including the temporal and spacial distribution of the brain and heart electrical currents. Recent successes in the development of chip-sized atomic clocks and magnetometers [39] provide a legitimate optimism for the creation of a small-size magnetic sensor. As a whole, the proposed EIT compass-magnetometer could find a broad variety of applications in physics, navigation, geology, biology, medicine, and industry.

ACKNOWLEDGMENTS

We thank L. Hollberg, H. Robinson, J. Kitching, F. Levi, S. Knappe, V. Shah, V. Gerginov, P. Schwindt, R. Wynands, I. Novikova, E. Mikhailov, Shura Zibrov, and Yiwen Chu for helpful discussions. V.I.Y. and A.V.T.

were supported by Russian Foundation for Basic Research (RFBR) (Grants No. 08-02-01108, No. 10-02-00591, and No. 10-08-00844) and programs of the Russian Academy of Sciences. V.L.V. and S.A.Z. were supported by RFBR (Grant No. 09-02-011151).

-
- [1] G. Alzetta, A. Gozzini, L. Moi, and G. Orriols, *Nuovo Cimento B* **36**, 5 (1976).
- [2] E. Arimondo, in *Progress in Optics*, edited by E. Wolf (Elsevier, Amsterdam, 1996), Vol. 35, p. 257.
- [3] S. E. Harris, *Phys. Today* **50**, 36 (1997).
- [4] M. Fleischhauer, M. A. Imamoglu, and J. P. Marangos, *Rev. Mod. Phys.* **77**, 633 (2005).
- [5] M. Fleischhauer and M. O. Scully, *Phys. Rev. A* **49**, 1973 (1994).
- [6] S. Pustelny, D. F. Jackson Kimball, S. M. Rochester, V. V. Yashchuk, W. Gawlik, and D. Budker, *Phys. Rev. A* **73**, 023817 (2006).
- [7] I. Novikova, A. B. Matsko, V. L. Velichansky, M. O. Scully, and G. R. Welch, *Phys. Rev. A* **63**, 063802 (2001).
- [8] M. Stähler, S. Knappe, C. Affolderbach, W. Kemp, and R. Wynands, *Europhys. Lett.* **54**, 323 (2001).
- [9] C. Affolderbach, M. Stähler, S. Knappe, and R. Wynands, *Appl. Phys. B* **75**, 605 (2002).
- [10] V. Acosta, M. P. Ledbetter, S. M. Rochester, D. Budker, D. F. Jackson Kimball, D. C. Hovde, W. Gawlik, S. Pustelny, J. Zachorowski, and V. V. Yashchuk, *Phys. Rev. A* **73**, 053404 (2006).
- [11] D. Budker and M. Romalis, *Nat. Phys.* **3**, 227 (2007).
- [12] I. K. Komonis, T. W. Kornack, J. C. Allred, and M. V. Romalis, *Nature (London)* **422**, 596 (2003).
- [13] A. J. Fairweather and M. J. Usher, *J. Phys. E* **5**, 986 (1972).
- [14] E. B. Alexandrov, M. V. Balabas, V. N. Kulyasov, A. E. Ivanov, A. S. Pazgalev, J. L. Raston, A. K. Vershovskii, and N. N. Yakobson, *Meas. Sci. Technol.* **15**, 918 (2004).
- [15] O. Gravrand, A. Khokhlov, J. L. Le Mouél, and J. M. Léger, *Earth Planets Space* **53**, 949 (2001).
- [16] R. Wynands, A. Nagel, S. Brandt, D. Meschede, and A. Weis, *Phys. Rev. A* **58**, 196 (1998).
- [17] H. Lee, M. Fleischhauer, and M. O. Scully, *Phys. Rev. A* **58**, 2587 (1998).
- [18] S. Pustelny, W. Gawlik, S. M. Rochester, D. F. Jackson Kimball, V. V. Yashchuk, and D. Budker, *Phys. Rev. A* **74**, 063420 (2006).
- [19] A. Weis, G. Bison, and A. S. Pazgalev, *Phys. Rev. A* **74**, 033401 (2006).
- [20] J. R. Torgerson, M. M. Schauer, S. K. Lamoreaux, and S. Gleyzes, *J. Opt. Soc. Am. B* **22**, 72 (2005).
- [21] E. B. Alexandrov and A. K. Vershovskii, *Phys. Usp.* **52**, 573 (2009).
- [22] A. V. Taichenachev, V. I. Yudin, V. L. Velichansky, A. S. Zibrov, and S. A. Zibrov, *Phys. Rev. A* **73**, 013812 (2006).
- [23] S. A. Zibrov, Y. O. Dudin, V. L. Velichansky, A. V. Taichenachev, and V. I. Yudin, in *Abstract Book and Technical Digest of ICONO-05, ISK8* (St. Petersburg, Russia, May 11–15, 2005).
- [24] A. V. Taichenachev, V. I. Yudin, V. L. Velichansky, and S. A. Zibrov, *JETP Lett.* **82**, 398 (2005).
- [25] S. A. Zibrov, V. L. Velichansky, A. S. Zibrov, A. V. Taichenachev, and V. I. Yudin, *JETP Lett.* **82**, 477 (2005).
- [26] E. Breschi, G. Kazakov, R. Lammegger, B. Matisov, L. Windholz, and G. Mileti, *IEEE Trans. Ultrason. Ferroelectr. Freq. Control* **56**, 926 (2009).
- [27] S. A. Zibrov, I. Novikova, D. F. Phillips, R. L. Walsworth, A. S. Zibrov, V. L. Velichansky, A. V. Taichenachev, and V. I. Yudin, *Phys. Rev. A* **81**, 013833 (2010).
- [28] E. E. Mikhailov, T. Horrom, N. Belcher, and I. Novikova, *J. Opt. Soc. Am. B* **27**, 417 (2010).
- [29] E. Arimondo, M. Inguscio, and P. Violino, *Rev. Mod. Phys.* **49**, 31 (1977).
- [30] D. A. Steck, Rubidium 87 D Line Data, available online at [<http://steck.us/alkalidata>] (revision 2.0.1, 2 May 2008).
- [31] E. B. Alexandrov, A. B. Mamyrin, and A. P. Sokolov, *Opt. Spektrosk. (USSR)* **34**, 1216 (1973).
- [32] M. D. Lukin, M. Fleischhauer, A. S. Zibrov, H. G. Robinson, V. L. Velichansky, L. Hollberg, and M. O. Scully, *Phys. Rev. Lett.* **79**, 2959 (1997).
- [33] E. E. Mikhailov, V. A. Sautenkov, Yu. V. Rostovtsev, A. Zhang, M. S. Zubairy, M. O. Scully, and G. R. Welch, *Phys. Rev. A* **74**, 013807 (2006).
- [34] A. S. Zibrov, A. B. Matsko, L. Hollberg, and V. L. Velichansky, *J. Mod. Opt.* **49**, 359 (2002).
- [35] G. Kazakov, B. Matisov, I. Mazets, G. Mileti, and J. Delporte, *Phys. Rev. A* **72**, 063408 (2005).
- [36] A. Ben-Kish and M. V. Romalis, e-print [arXiv:1001.0345](https://arxiv.org/abs/1001.0345) (2010).
- [37] G. Bison, R. Wynands, and A. Weis, *Appl. Phys. B* **76**, 325 (2003).
- [38] G. Bison, R. Wynands, and A. Weis, *Opt. Express* **11**, 904 (2003).
- [39] P. Schwindt, S. Knappe, V. Shah, L. Hollberg, J. Kitching, L. Liew, and L. Moreland, *Appl. Phys. Lett.* **85**, 6409 (2004).